Graphene MEMS resonator: model formulation and computational investigation

Abdulaziz Sultan Abdullah

abdulazeizsultan92@gmail.com

ABSTRACT

This study investigates the static and time-dependent response of graphene-based cantilever beam resonators when subjected to electrostatic forces applied at their free ends. A detailed examination of the system's behavior is carried out, where the nonlinear governing relation is derived through the energy approach in conjunction with Hamilton's principle. An explicit analytical expression for the nonlinear static case is presented. In addition, the effective stiffness coefficient for a lumped-parameter model of the cantilever beam loaded at its tip is determined, which provides the basis for a thorough exploration of the system's dynamics. Special emphasis is placed on the onset of dynamic pull-in phenomena under both steady and oscillatory excitations, with analytical forecasts confirmed by numerical computations. The findings indicate that the system maintains periodic oscillations whenever the excitation parameters remain below a critical threshold defined by a separatrix curve. Once the parameters surpass this limit, pull-in instability takes place, leading the beam to collapse onto the substrate. Furthermore, the effect of excitation frequency on the resonator's behavior under harmonic loading is assessed. Simulation results demonstrate that selecting a frequency close to the natural resonance of the beam may, under specific parameter ranges, induce structural failure.

Keywords

MEMS, graphene-based resonator, dynamic pull-in instability, periodic oscillations, singular MEMS systems.

1 Introduction

Microelectromechanical systems (MEMS) have transformed a wide range of technologies by making it possible to engineer miniaturized devices with exceptional efficiency and multifunctionality. Their key strengths include compact geometry, minimal energy demand, and the ability to merge electrical, mechanical, and optical operations on a single substrate [1]. Within MEMS, microresonators are critical elements since they operate close to their natural frequencies. Such devices are extensively used in ultra-sensitive sensing technologies, such as protein detection [2], molecular analysis [3], electron measurements, and nanoparticle identification [4]. Nonetheless, the performance of these sensors is often constrained by the intrinsic mass of the resonator itself, as the smallest detectable load depends directly on it. For this reason, ultralight, mechanically robust materials are essential. Graphene has emerged as a breakthrough option because of its very low density combined with extraordinary strength and stiffness, making it highly suitable for MEMS microresonators. Table 1 compares its mechanical behavior with that of conventional MEMS materials like silicon and steel.

Graphene consists of a single atomic layer of carbon atoms arranged in a tightly bonded hexagonal lattice. Its unique mechanical robustness arises from the sp^2 carbon–carbon bonding structure [5]. In addition to strength, graphene possesses remarkable electronic behavior, which has positioned it as a candidate for spintronics and pseudospintronics, as described by Pesin and MacDonald [6]. The material exhibits a Young's modulus approaching 2 TPa [7], tensile strength far greater than the toughest steel [8], and ductility that permits stretching up to about 20% [9]. These attributes enable applications ranging from transparent conductors and flexible composites to stretchable electronic displays and high-capacity energy storage devices [10]. Moreover, its distinctive topological features, including conical singularities and bound states, have been studied for their potential in novel nanostructures, as highlighted in Rüegg and Lin [11].

Although graphene was once considered non-piezoelectric due to its inherent lattice symmetry, recent progress has demonstrated its use in MEMS/NEMS for energy harvesting,

actuation, and signal transduction [12]. Its exceptionally small mass and responsiveness also make it highly attractive for ultra-precise mass sensing. With a thermal conductivity reaching ~500 $Wm^{-1}K^{-1}$ at room temperature [14], it shows strong potential in thermal management applications as well. Long-term integration in devices, however, requires stable adhesion with substrates, while its friction-reducing and corrosion-resistant tribological properties add further advantages [10, 15].

These extraordinary characteristics of graphene pave the way for pushing MEMS resonators to even smaller scales. In fact, graphene-based mass sensors are increasingly studied as nonlinear effects in vibrations can enhance their detection capabilities, as shown in [16]. Nonlinear analytical methods, previously employed in wave propagation and system stability studies, have also been adapted for graphene resonators [17]. For example, Natsuki et al. demonstrated that dual-layer graphene sheets provide greater sensitivity than single-layer ones [18], while Karličić et al. [19] reported that tuning magnetic fields could further shift resonance frequencies and improve sensitivity. In addition to experimental explorations, a significant body of work focuses on mathematical modeling. Wei et al. analyzed the steady response of a graphene Euler beam under uniform loading and provided both analytical and finite element solutions [20]. Approximate finite element formulations derived from the Rayleigh–Ritz approach with Hermite interpolation also matched the analytical results.

The dynamic aspects of graphene-based devices under electrostatic actuation have attracted significant research attention. Notable investigations include those by Anjum and He [21], Kadyrov et al. [22], Skrzypacz et al. [23], Wei et al. [24], and Omarov et al. [25]. Insights from nonlinear Schrödinger-type soliton models [26] may also inform analytical strategies for MEMS resonator dynamics. Electrostatic actuation remains the most widely used method in MEMS, outperforming thermal, piezoelectric, or electromagnetic methods in terms of simplicity and energy efficiency [1, 27]. In electrostatically driven cantilever beams, the applied voltage usually contains both DC and AC components: the DC bias shifts the equilibrium position of the beam, while the AC input produces oscillations about that equilibrium. Stability is achieved when the elastic restoring force equals the applied electrostatic attraction [1].

If the DC voltage surpasses a critical level, the electrostatic force overwhelms the elastic restoring capacity, forcing the beam to collapse onto an adjacent electrode. This is identified as the *pull-in phenomenon*, with the associated threshold referred to as the pull-in voltage. Two distinct categories exist: static pull-in, driven purely by DC bias, and dynamic pull-in, triggered by harmonic excitation or system motion. Controlling these instabilities is vital to MEMS design because uncontrolled pull-in leads to failure. Skrzypacz et al. [23] derived necessary and sufficient conditions for the existence of periodic orbits in a lumped mass MEMS model subjected to constant bias. Studies by Kadyrov et al. [22] and Omarov et al. [25] further expanded this analysis by examining harmonic excitation, with Omarov et al. employing Sturm's theorem to classify periodic solutions and verifying results numerically using Python. Meanwhile, Anjum and He [21] and Wei et al. [24] studied the nonlinear beam equations governing graphene resonators and uncovered multiple natural frequencies through the variational iteration method.

Table 1. Mechanical parameters of graphene compared with steel and silicon

Material	Young's modulus (GPa)	Tensile strength (GPa)
Graphene	2000 ± 400 [7]	130 ± 10 [33]
Steel	200 [39]	0.25 [40]
Silicon	130–169 [41]	7 [42]

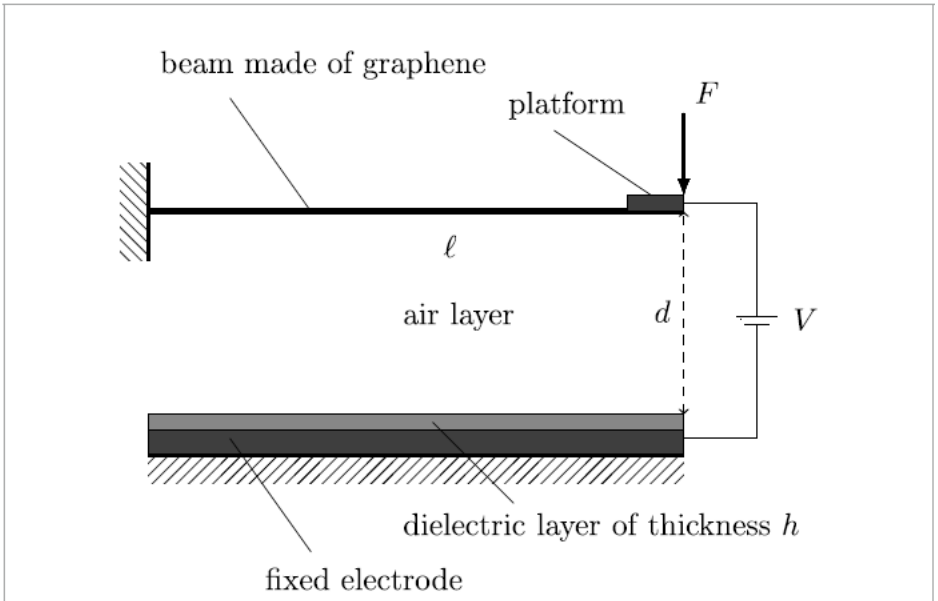

FIGURE 1
A schematic of a graphene microresonator.

Approximation strategies such as the Laplace transform in combination with Padé approximants have been employed to derive near-exact solutions for nonlinear oscillatory systems. More recent applications of approximation methods targeting periodic responses of MEMS oscillators are illustrated in He [28], while the collapse behavior of nonlinear quadratic oscillators has been analyzed in He et al. [29]. Parallel research on nonlinear wave equations has revealed that higher-order dispersion mechanisms significantly influence both stability and the dynamic response of such systems, as discussed by Li and Fajun [30].

In this paper, attention is directed toward the static and dynamic response of a graphene cantilever beam operated under electrostatic loading applied at its free end. The model framework follows the formulation of Skrzypacz et al. [31], where the system is represented by a lightweight graphene cantilever of length ℓ, coupled with a rigid electrode platform attached to its tip, positioned opposite to a grounded electrode coated with a

dielectric layer of thickness h and relative permittivity εr (see Figure 1). The separation distance d and the potential difference V between the electrodes determine the electrostatic attraction. The competition between this attraction and the nonlinear restoring action of the beam is predicted to produce high-frequency oscillatory behavior. Furthermore, the influence of nonlocal interactions in phononic lattices—structures with characteristics resembling graphene resonators—has been examined for their effects on localized modes and wave transmission, as shown by Poggetto et al. [32].

The structure of this study is as follows:

- **Section 2** derives the governing nonlinear equation of motion using Hamilton's principle and the energy approach, along with the associated boundary conditions.
- **Section 3** addresses the analytical solution for the static equilibrium configuration.
- **Section 4** develops a lumped-parameter model to explore the essential dynamic characteristics of the cantilever system, including the determination of the generalized stiffness coefficient for tip loading.
- **Section 5** is dedicated to analyzing pull-in instability under both steady and oscillatory excitation.
- **Section 6** presents numerical simulations highlighting the system's resonance and dynamic pull-in scenarios.
- **Section 7** concludes with key findings and implications of the study.

2.1 Stress–strain formulation for graphene

Both theoretical considerations and experimental observations confirm that the stress–strain law for a graphene beam following Euler–Bernoulli theory can be expressed as:

$$\sigma = E\varepsilon + D \mid \varepsilon \mid \varepsilon, \qquad (1)$$

where $\sigma$is the stress, $\varepsilon$the strain, and Edenotes Young's modulus. The parameter $D = -\frac{E^2}{4\sigma_{\max}}$represents the second-order elastic stiffness coefficient [33, 34]. A negative value of Dindicates a reduction in stiffness under strong tensile loading, while compressive loading leads to stiffening.

Khan et al. [35] experimentally obtained values for $E$and $D$by conducting nanoindentation tests with an atomic force microscope on monolayer graphene sheets. Their results indicated $E = 2.4 \pm 0.04$TPa and $D = -2.0 \pm 0.4$TPa. Lee et al. [33] further explained that the nonlinear character of the stress–strain curve in graphene originates from the third-order contribution of the strain-dependent energy potential expanded in a Taylor series.

This constitutive stress–strain model will serve as the basis for the mathematical developments presented in the next section.

2.2 Governing equation for a graphene Euler–Bernoulli beam

We examine a cantilever beam subjected to a tip force and consider an infinitesimal segment before and after bending (see Figure 2). Let the transverse displacement of the beam be denoted as $w = w(x, t)$, where $t$is time and $x$is the axial coordinate. In line with Euler–Bernoulli assumptions, cross-sections of the beam remain flat and perpendicular to the neutral axis throughout deformation [1].

Consider a point Bpositioned a distance $y$away from the neutral axis. Its axial displacement due to bending is given by

$$u_b = -yw',$$

so that the corresponding axial strain is

$$\varepsilon_b = \frac{\partial u_b}{\partial x} = -yw''.$$

Using the constitutive relation (Eq. 1) and integrating with respect to strain, the strain energy density is obtained, which represents the energy stored per unit volume from deformation:

$$U = \frac{1}{2}E\varepsilon\varepsilon^T + \frac{1}{3}D \mid \varepsilon \mid \varepsilon\varepsilon^T. \qquad (2)$$

Here, $\varepsilon = (\varepsilon_x, \varepsilon_y, \varepsilon_z, \gamma_{xy}, \gamma_{xz}, \gamma_{yz})$denotes the strain tensor, with

$$\varepsilon_x = \frac{\partial u}{\partial x}, \varepsilon_y = \frac{\partial w}{\partial y}, \varepsilon_z = \frac{\partial v}{\partial z}, \gamma_{xy} = \frac{1}{2}(\frac{\partial u}{\partial y} + \frac{\partial w}{\partial x}),$$
$$\gamma_{xz} = \frac{1}{2}(\frac{\partial u}{\partial z} + \frac{\partial v}{\partial x}), \gamma_{yz} = \frac{1}{2}(\frac{\partial w}{\partial z} + \frac{\partial v}{\partial y}).$$

For an Euler–Bernoulli beam, only the axial strain component $\varepsilon_x$is relevant, so that

$$\varepsilon_x = -yw'' = \varepsilon_b, \varepsilon_y = \varepsilon_z = \gamma_{xy} = \gamma_{xz} = \gamma_{yz} = 0.$$

Substituting into Eq. (2) yields

$$U = \frac{1}{2}E\varepsilon_x^2 + \frac{1}{3}D \mid \varepsilon_x \mid \varepsilon_x^2.$$

The total potential energy is obtained by integrating over the beam's volume V:

$$E_{\text{pot}} = \frac{1}{2}\int_V E\varepsilon_x^2 \, dV + \frac{1}{3}\int_V D \mid \varepsilon_x \mid \varepsilon_x^2 \, dV. \qquad (3)$$

Substituting $\varepsilon_x = -yw''$into Eq. (3) gives

$$E_{\text{pot}} = \frac{1}{2}\int_V E(yw'')^2 \, dV + \frac{1}{3}\int_V D \mid w'' \mid (w'')^2 y^3 \, dV.$$

This can be decomposed into

$$E_{\text{pot}}^{(1)} = \frac{1}{2}\int_0^\ell E(w'')^2 (\int_A y^2 \, dA)dx = \frac{EI_1}{2}\int_0^\ell (w'')^2 dx, \qquad (5)$$
$$E_{\text{pot}}^{(2)} = \frac{1}{3}\int_0^\ell D \mid w'' \mid (w'')^2 (\int_A y^3 \, dA)dx = \frac{DI_2}{3}\int_0^\ell \mid w'' \mid (w'')^2 dx, \qquad (7)$$

where $I_1 = \int_A y^2 \, dA$is the second moment of inertia and $I_2 = \int_A y^3 \, dA$is the third moment of inertia of the cross section.

Thus, the full potential energy expression is

$$E_{\text{pot}} = \frac{EI_1}{2}\int_0^\ell (w'')^2 dx + \frac{DI_2}{3}\int_0^\ell \mid w'' \mid (w'')^2 dx.$$

The kinetic energy of the beam, based on distributed mass ρA, is given by

$$E_{\text{kin}} = \frac{\rho A}{2} \int_0^{\ell} \dot{w}^2 dx,$$

with $\dot{w} = \partial w / \partial t$.

Finally, the external work from a tip load Fapplied at $x = \ell$is expressed as

$$W = Fw(\ell).$$

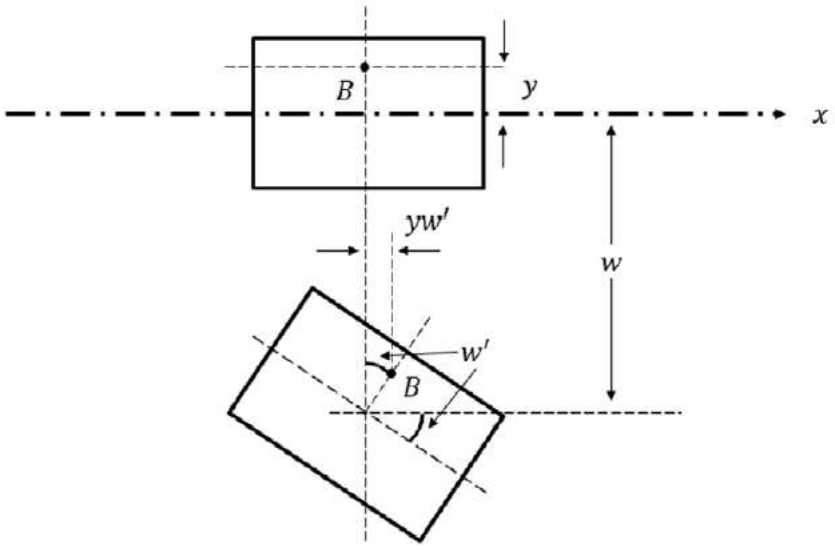

FIGURE 2
A segment of a beam before and after bending.

2.3 Application of Hamilton's principle

To derive the governing equation of motion for the graphene cantilever beam, we employ Hamilton's principle together with the Lagrangian functional [1, 36]. The Lagrangian is defined as

$$I(w) = E_{\text{kin}}(w) - E_{\text{pot}}(w) + W(w),$$

where $E_{\text{kin}}$is the kinetic energy, $E_{\text{pot}}$the potential energy, and $W$the work of the external force.

According to Hamilton's principle, the variation of the action integral satisfies

$$\int_{t_1}^{t_2} \delta I(w)\, dt = \int_{t_1}^{t_2} [\delta E_{\text{kin}}(w) - \delta E_{\text{pot}}(w) + \delta W(w)]\, dt = 0, \qquad (8)$$

for two arbitrary instants $t_1$and t_2, with δdenoting the variation operator. This requires evaluating the variations of each energy contribution in terms of the virtual displacement δw.

The variation of the external work is

$$\delta W = F\, \delta w(\ell),$$

and the variation of kinetic energy is

$$\delta E_{\text{kin}} = \rho A \int_0^{\ell} \dot{w}\, \delta \dot{w}\, dx. \qquad (9)$$

Integrating in time gives

$$\int_{t_1}^{t_2} \delta E_{\text{kin}}\, dt = \rho A \int_0^{\ell} [\dot{w}\delta w\, |_{t_1}^{t_2} - \int_{t_1}^{t_2} \ddot{w}\, \delta w\, dt]\, dx. \qquad (10)$$

Since the virtual displacement is zero at the time boundaries ($\delta w(t_1) = \delta w(t_2) = 0$), the boundary term vanishes, leaving only the integral term.

The variation of the potential energy, from Eq. (4), is

$$\delta E_{\text{pot}} = EI_1 \int_0^{\ell} w''\, \delta w''\, dx \;+\; DI_2 \int_0^{\ell} |\, w''\, |\, w''\, \delta w''\; dx. \qquad (11)$$

Using integration by parts, these terms can be rewritten:

$$EI_1 \int_0^{\ell} w''\delta w''\, dx = EI_1[w''\delta w'\, |_0^{\ell} - w'''\delta w\, |_0^{\ell} + \int_0^{\ell} w^{(4)}\delta w\, dx], \qquad (12)$$

$$DI_2 \int_0^{\ell} |\, w''\, |\, w''\delta w''\, dx = DI_2[|\, w''\, |\, w''\delta w'\, |_0^{\ell} - (|\, w''\, |\, w'')'\delta w\, |_0^{\ell} + \int_0^{\ell} |\, w''\, |\, w'')''\delta w\, dx]\,(.$$

Substituting (12) and (13) into Eq. (8) and grouping terms leads to

$$\int_{t_1}^{t_2} \{\int_0^{\ell} [-\rho A\ddot{w} - EI_1 w^{(4)} - DI_2(|\, w'' \,|\, w'')'']\delta w\, dx$$
$$-[EI_1 w'' + DI_2 \,|\, w'' \,|\, w'']\delta w' \,|_0^{\ell} + [EI_1 w''' + DI_2(|\, w'' \,|\, w'')' + F]\delta w(\ell) - [EI_1 w''' + DI_2(|\, w'' \,|\, w$$

Since $\delta w$is arbitrary, each group of terms must vanish independently, yielding the governing equation of motion:

$$\rho A\ddot{w} + EI_1 w^{(4)} + DI_2(|\, w'' \,|\, w'')'' = 0,$$

with boundary conditions

$$w(t,0) = 0, w'(t,0) = 0, \qquad (17)$$
$$EI_1 w''' + DI_2(|\, w'' \,|\, w'')' = 0 \text{at } x = 0,$$
$$EI_1 w''' + DI_2(|\, w'' \,|\, w'')' = -F \text{at } x = \ell,$$
$$EI_1 w'' + DI_2 \,|\, w'' \,|\, w'' = 0 \text{at } x = \ell. \qquad (16)$$

Thus, Hamilton's principle provides both the beam's nonlinear equation of motion and its boundary conditions for a graphene cantilever under tip loading.

3 Analytical solution for the static case

Consider a point load $F(x) = F$applied at the free end of the cantilever. The governing differential equation of the beam under this tip load is

$$EI_1 w^{(4)} + DI_2(|\, w'' \,|\, w'')'' = 0, 0 < x < \ell, \qquad (18)$$

subject to the boundary conditions

$$w(0) = 0, \qquad (19)$$
$$w'(0) = 0, \qquad (20)$$
$$(EI_1 + DI_2 \,|\, w'' \,|)w'' \,|_{x=\ell} = 0, \qquad (21)$$
$$(EI_1 w''' + DI_2(|\, w'' \,|\, w'')') \,|_{x=\ell} = -F. \qquad (22)$$

By integrating Eq. (18) twice and imposing the tip conditions (21)–(22), the reduced form becomes

$$(EI_1 + DI_2 \mid w'' \mid)w'' = -F(x-\ell), 0 < x < \ell. \qquad (23)$$

Since the right-hand side of Eq. (23) is nonnegative for $F \geq 0$, the left-hand side must also remain nonnegative. For a downward-deflecting cantilever under a positive tip force, the deflection curve is concave, implying $w'' < 0$. Hence, Eq. (23) reduces to

$$EI_1 w'' - DI_2 (w'')^2 = -F(x-\ell).$$

Solving for w''yields

$$w'' = \frac{EI_1 \pm \sqrt{(EI_1)^2 - 4DI_2 F(x-\ell)}}{2DI_2}. \qquad (24)$$

A physically meaningful solution exists only if the applied force is below a certain threshold, namely

$$F \leq \frac{(EI_1)^2}{4 \mid D \mid I_2 \ell}.$$

Condition (21) is satisfied only for the minus root, giving

$$w'' = \frac{EI_1 - \sqrt{(EI_1)^2 - 4DI_2 F(x-\ell)}}{2DI_2}. \qquad (25)$$

Integrating Eq. (25) once provides

$$w' = \frac{EI_1}{2DI_2} x + \frac{((EI_1)^2 - 4DI_2 F(x-\ell))^{3/2}}{12(DI_2)^2 F} + C_1,$$

and a second integration gives

$$w = \frac{EI_1}{4DI_2} x^2 - \frac{((EI_1)^2 - 4DI_2 F(x-\ell))^{5/2}}{120(DI_2)^3 F^2} + C_1 x + C_2.$$

The constants $C_1$and C_2follow from the clamped-end conditions (19)–(20), resulting in

$$C_1 = -\frac{((EI_1)^2 + 4DI_2 F\ell)^{3/2}}{12(DI_2)^2 F},$$

$$C_2 = \frac{((EI_1)^2 + 4DI_2 F\ell)^{5/2}}{120(DI_2)^3 F^2}.$$

Thus, the closed-form static deflection of the graphene beam under a tip load is

$$w(x) = \frac{EI_1}{4DI_2}x^2 - \frac{((EI_1)^2 - 4DI_2F(x-\ell))^{5/2}}{120(DI_2)^3F^2} - \frac{((EI_1)^2 + 4DI_2F\ell)^{3/2}}{12(DI_2)^2F}x + \frac{((EI_1)^2 + 4DI_2F\ell)^{5/2}}{120(DI_2)^3F^2}.$$

When the nonlinear stiffness coefficient $D \to 0$, this solution simplifies to the well-known Euler–Bernoulli expression for a linearly elastic cantilever beam subjected to a point force at its tip. That classical result assumes small deflections, uniform cross section, and a transverse load applied perpendicular to the beam axis. A detailed derivation is included in the Supplementary Appendix.

4 Galerkin Approximation

4.1 Equivalent Lumped Mass Model

The transverse vibration of the graphene beam along $x \in [0, \ell]$at time $t > 0$is governed by:

$$\rho A\ddot{w}(t,x) + EI_1 w^{(4)}(t,x) + DI_2(\mid w''(t,x) \mid w''(t,x))'' = 0, \qquad (27)$$

with the boundary and initial conditions:

$$w(t,0) = 0, \qquad (28)$$

$$w'(t,0) = 0, \qquad (29)$$

$$(EI_1 + DI_2 \mid w''(t,\ell) \mid)w''(t,\ell) = 0, \qquad (30)$$

$$EI_1 w'''(t,\ell) + DI_2(\mid w''(t,\ell) \mid w''(t,\ell))' = -F_E, \qquad (31)$$

$$w(0,x) = 0, \dot{w}(0,x) = 0,$$

where the electrostatic load is given by:

$$F_E = \frac{\varepsilon_0 V^2 S}{2(d + h/\varepsilon_r - w(t,\ell))^2}.$$

Assuming the deformation remains small and the geometry is simple, a single-mode Galerkin expansion is adopted:

$$w(x,t) \approx X(t)Y(x),$$

where $X(t)$is a generalized coordinate and $Y(x)$is a trial shape function satisfying the cantilever boundary conditions, $Y(0) = Y'(0) = 0$.

Multiplying Eq. (27) by $Y(x)$, integrating over $[0, \ell]$, and applying the boundary conditions (28)–(31) yields:

$$\frac{1}{Y(\ell)}\int_0^{\ell} \rho A\ddot{w}(t,x)Y(x)dx + \frac{1}{Y(\ell)}\int_0^{\ell} EI_1 w''(t,x)Y''(x)dx + \frac{1}{Y(\ell)}\int_0^{\ell} DI_2(|\, w''(t,x)\,|\, w''(t,x)$$

This reduces to the Galerkin equation:

$$m_1\ddot{X}(t) + k_1X(t) + k_2\,|\,X(t)\,|\,X(t) = \frac{\varepsilon_0 V^2 S}{2(d + h/\varepsilon_r - X(t)Y(\ell))^2}, \qquad (33)$$

where the effective parameters are:

$$m_1 = \frac{\rho A}{Y(\ell)}\int_0^{\ell} Y^2(x)dx, k_1 = \frac{EI_1}{Y(\ell)}\int_0^{\ell} (Y''(x))^2dx, k_2 = \frac{DI_2}{Y(\ell)}\int_0^{\ell} |\,Y''(x)\,|\,(Y''(x))^2dx. \qquad (34$$

Here, $m_1$acts as the equivalent mass of the beam, while $k_1$and $k_2$represent the linear and nonlinear stiffness coefficients.

4.2 Dimensionless Single-Degree-of-Freedom Model

Following Skrzypacz et al. [37], the scaled first eigenfunction of the cantilever beam is chosen as the trial function:

$$\hat{Y}(x) = \frac{1}{2}(\hat{Y}_3(x,\mu_1) - \frac{\hat{Y}_1(1,\mu_1)}{\hat{Y}_2(1,\mu_1)}\hat{Y}_4(x,\mu_1)),$$

where

$$\hat{Y}_1(x,\mu) = \cosh(\mu x) + \cos(\mu x), \hat{Y}_2(x,\mu) = \sinh(\mu x) + \sin(\mu x),$$
$$\hat{Y}_3(x,\mu) = \cosh(\mu x) - \cos(\mu x), \hat{Y}_4(x,\mu) = \sinh(\mu x) - \sin(\mu x).$$

The spectral parameter $\mu_1$is the first positive solution of:

$$1 + \cosh(\mu)\cos(\mu) = 0.$$

Thus, the Galerkin ansatz uses $Y(x) = \hat{Y}(x/\ell)$, ensuring that $Y(0) = Y'(0) = 0$and $Y''(\ell) = Y'''(\ell) = 0$.

From [37], the following integrals hold:

$$\int_0^1 \hat{Y}^2(x)dx = \frac{1}{4}, \int_0^1 (\hat{Y}''(x))^2 dx = \frac{\mu_1^4}{4}.$$

This implies:

$$\int_0^\ell Y^2(x)dx = \frac{\ell}{4}, \int_0^\ell (Y''(x))^2 dx = \frac{\mu_1^4}{4\ell^3}.$$

Numerical evaluation gives:

$$\int_0^1 (\hat{Y}''(x))^3 dx = 8.02945400733,$$

so that

$$\int_0^\ell (Y''(x))^3 dx = \frac{8.02945400733}{\ell^5}.$$

The effective coefficients are therefore:

$$m_1 = \frac{m}{4}, k_1 = \frac{EI_1\mu_1^4}{4\ell^3}, k_2 = \frac{8.02945400733DI_2}{\ell^5}, \qquad (35)$$

where $m$is the total mass of the beam and $\mu_1 = 1.8751040687$.

Introducing the nondimensional variables:

$$\tau = \frac{t}{\ell^2}\sqrt{\frac{EI_1\mu_1^4}{\rho A}}, y = \frac{X}{d + h/\varepsilon_r}, \qquad (36)$$

Eq. (33) becomes:

$$\ddot{y} + y + \alpha \mid y \mid y = \frac{\lambda}{(1-y)^2}, \qquad (38)$$

with initial conditions

$$y(0) = 0, \dot{y}(0) = 0,$$

where

$$\alpha = \frac{k_2}{k_1}(d + h/\varepsilon_r), \lambda(\tau) = \frac{\varepsilon_0 K^2(\tau) S}{2k_1(d + h/\varepsilon_r)^3},$$

and

$$K(\tau) = V(\tau\ell^2 \sqrt{\frac{\rho A}{E I_1 \mu_1^4}}).$$

5 . Pull-in and Resonance

5.1 Constant Voltage Excitation

In this part, we analyze the *dynamic pull-in instability* of the lumped-mass formulation (Eq. 48) when the cantilever is biased with a constant DC voltage. The investigation relies on a **phase-plane approach**, which clearly distinguishes between regions of periodic oscillations and those where collapse (pull-in) takes place.

Earlier studies [23] established that the nondimensional equation

$$\ddot{y} + y + \alpha \mid y \mid y - \frac{\lambda}{(1-y)^2} = 0, \qquad (39)$$

admits bounded oscillatory solutions when $\alpha \leq 0$and $\lambda > 0$. To examine its qualitative dynamics, we recast the system in the $(y, \dot{y})$-plane. Multiplying Eq. (39) by $\dot{y}$and integrating with respect to τgives an energy conservation law:

$$E(\tau) = \frac{1}{2}(\dot{y}(\tau))^2 + \frac{1}{2}y^2(\tau) + \frac{1}{3}\alpha \mid y(\tau) \mid y^2(\tau) - \frac{\lambda}{1-y(\tau)} = C. \qquad (40)$$

The integration constant Cfollows from the initial conditions (Eq. 38), yielding $C = -\lambda$. Substituting this into Eq. (40) provides the equivalent form:

$$(\dot{y})^2 = -y^2 - \frac{2}{3}\alpha \mid y \mid y^2 + \frac{2\lambda}{1-y} - 2\lambda. \qquad (41)$$

The structure of Eq. (41) determines the shape of the **phase portrait**. If the right-hand side admits roots within $y \in (0,1)$, the trajectories form closed loops corresponding to periodic solutions (limit cycles). Conversely, if no such roots exist, the beam undergoes pull-in collapse.

The boundary separating these regimes is the **separatrix curve**, which defines the threshold between oscillatory behavior and instability. To derive this separatrix, we denote the right-hand side of Eq. (41) as

$$f_{\alpha,\lambda}(y) = -y^2 - \frac{2}{3}\alpha y^3 + \frac{2\lambda}{1-y} - 2\lambda = \frac{y(\frac{2}{3}\alpha y^3 - (\frac{2}{3}\alpha - 1)y^2 - y + 2\lambda)}{1-y}. \quad (42)$$

Equation (42) has up to four roots: one negative root outside $(0,1)$, the trivial root at $y = 0$, and at most two within the open interval $(0,1)$. The cubic polynomial

$$h_{\alpha,\lambda}(y) = \frac{2}{3}\alpha y^3 - (\frac{2}{3}\alpha - 1)y^2 - y + 2\lambda \quad (43)$$

shares the same interior roots. Tangency with the horizontal axis occurs when both

$$h_{\alpha,\lambda}(y^*) = 0, h'_{\alpha,\lambda}(y^*) = 0$$

for some $y^* \in (0,1)$. Solving the derivative condition gives

$$h'_{\alpha,\lambda}(y) = 2\alpha y^2 - 2(\frac{2}{3}\alpha - 1)y - 1 = 0,$$

with solutions

$$y^*_{1,2} = \frac{(\frac{2}{3}\alpha - 1) \pm \sqrt{(\frac{2}{3}\alpha - 1)^2 + 2\alpha}}{2\alpha}.$$

Only

$$y^* = \frac{(\frac{2}{3}\alpha - 1) + \sqrt{(\frac{2}{3}\alpha - 1)^2 + 2\alpha}}{2\alpha}$$

falls within $(0,1)$. Hence, the system supports periodic motion provided that

$$h_{\alpha,\lambda}(y^*) \leq 0.$$

Expanding yields

$$h_{\alpha,\lambda}(y^*) = \frac{1}{162\alpha^2}(-8\alpha^3 + \alpha(27 - 6\nu) - 9(-3 + \nu) - 2\alpha^2(9 + 2\nu - 162\lambda)) \leq 0,$$

with

$$\nu = \sqrt{9 + 6\alpha + 4\alpha^2}.$$

Rearranging gives the separatrix function:

$$\lambda \leq \kappa(\alpha) = -\frac{1}{324\alpha^2}(-8\alpha^3 + \alpha(27 - 6\nu) - 9(-3 + \nu) - 2\alpha^2(9 + 2\nu)). \quad (44)$$

The operational chart in Figure 4 illustrates that points (α, λ)lying above the separatrix $\kappa(\alpha)$lead to pull-in collapse, while those below correspond to stable oscillations.

Thus, the **critical pull-in voltage** is given explicitly by

$$V_{\text{pull-in}} = \sqrt{\frac{2k_1(d + h/\varepsilon_r)^3\kappa(\alpha)}{\varepsilon_0 S}}.$$

In addition, the **pull-in time**—the duration until the structure collapses under electrostatic loading—is a key measure of device reliability and will be addressed in the following analysis.

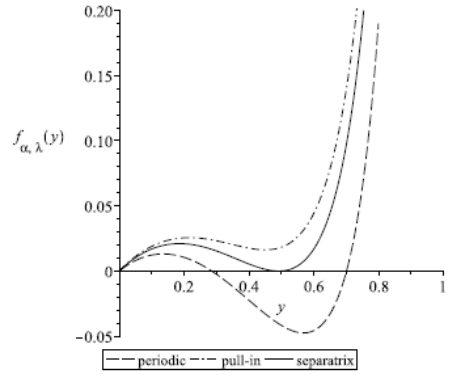

FIGURE 3
The separatrix occurs when the potential function $f_{\alpha,\lambda}(y)$ is tangent to the horizontal axis.

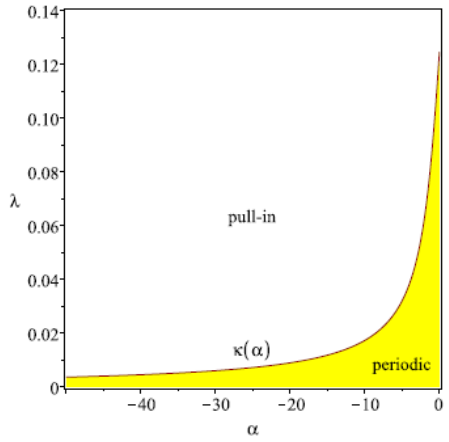

FIGURE 4
Parameter regions for pull-in and periodic solutions.

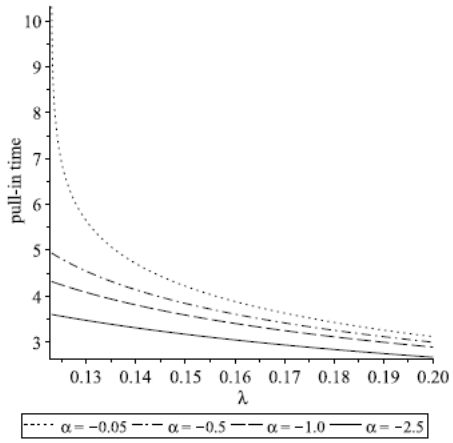

FIGURE 5
Pull-in times for various values of parameter α.

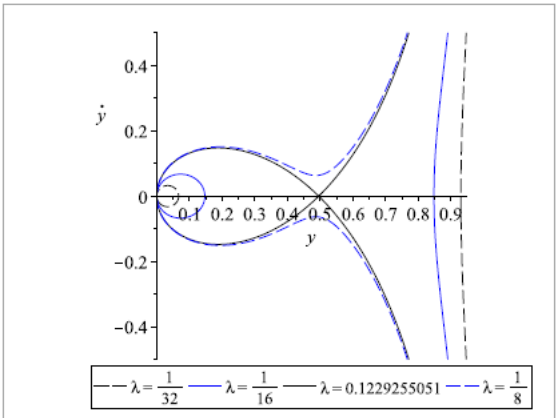

a. Phase trajectories for $\alpha = -0.05$ and various values of λ.

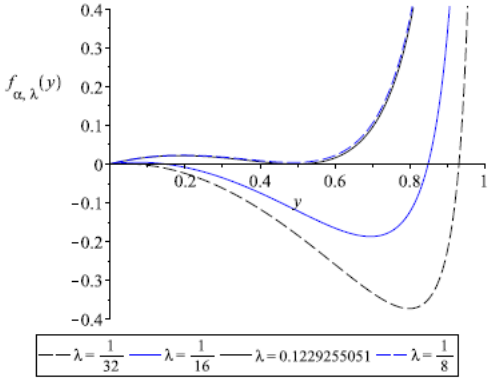

b. Corresponding potential energy functions.

FIGURE 6
(a) Phase trajectories for $\alpha = -0.05$ and various values of λ and **(b)** corresponding potential energy functions.

The velocity of the cantilever tip for a given parameter λcan be written as

$$\dot{y} = \frac{dy}{dt} = \sqrt{-y^2 - \frac{2}{3}\alpha y^3 + \frac{2\lambda}{1-y} - 2\lambda}. \qquad (45)$$

From this, the **pull-in time** $t_{\text{pull-in}}$is obtained as

$$t_{\text{pull-in}} = \int_0^1 \frac{dy}{\sqrt{-y^2 - \frac{2}{3}\alpha y^3 + \frac{2\lambda}{1-y} - 2\lambda}}. \qquad (46)$$

The integral (46) represents the time required for the beam's free end to move from its initial equilibrium to contact with the fixed electrode, which marks the onset of pull-in. Figure 5 illustrates how the excitation parameter λinfluences the collapse time for different values of α. As expected, increasing λshortens the pull-in time for a fixed α.

In the same spirit, the **oscillation period** Tcan be derived. Integrating (45) between $y = 0$and the oscillation amplitude $y_{\max}$, and doubling the result gives:

$$T = 2\int_0^{y_{\max}} \frac{dy}{\sqrt{-y^2 - \frac{2}{3}\alpha y^3 + \frac{2\lambda}{1-y} - 2\lambda}}, \qquad (47)$$

where $y_{\max} \in (0,1)$is the maximum displacement amplitude, obtained as a root of the cubic function $h_{\alpha,\lambda}(y)$. Phase-plane trajectories and potential energy plots (Figures 6–9) illustrate these oscillatory amplitudes.

A more general setting involves an applied **time-dependent voltage**, studied in [22], expressed as

$$V(t) = V_{\text{DC}} + V_{\text{AC}}\cos(\Omega t), \qquad (48)$$

with excitation frequency $\Omega$and period $T = \frac{2\pi}{\Omega}$. Kadyrov et al. established a theorem for such systems: if $c \geq 0$is a constant, $h(x)$is a continuous real function on $(-\infty, 1]$, and $V(t)$is a periodic function, then the nonlinear second-order differential equation

$$\ddot{y} + c\dot{y} + h(y) - \frac{V^2(t)}{(1-y)^2} = 0 \qquad (49)$$

admits a periodic solution provided

$$h(y) = \frac{V_M^2}{(1-y)^2},$$

where V_M denotes the maximum of $V(t)$.

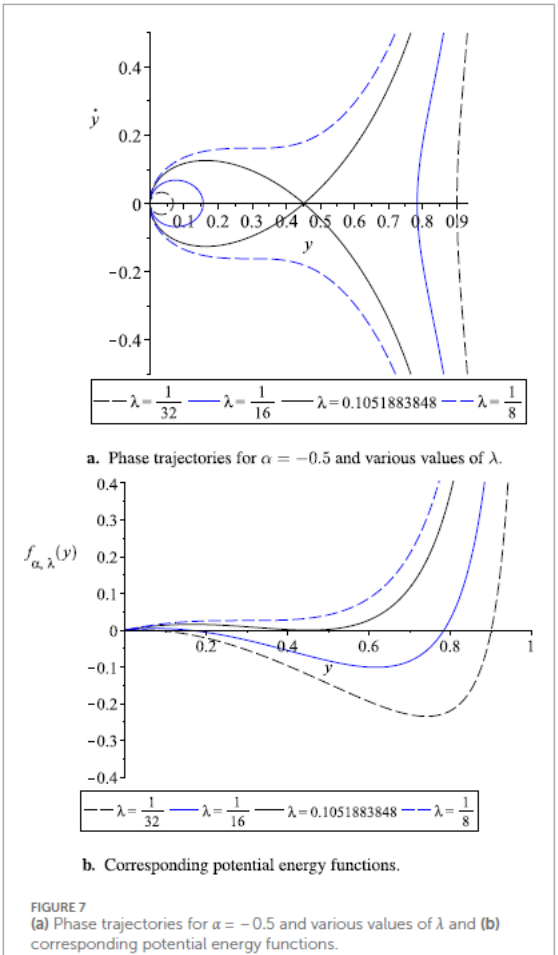

a. Phase trajectories for $\alpha = -0.5$ and various values of λ.

b. Corresponding potential energy functions.

FIGURE 7
(a) Phase trajectories for $\alpha = -0.5$ and various values of λ and (b) corresponding potential energy functions.

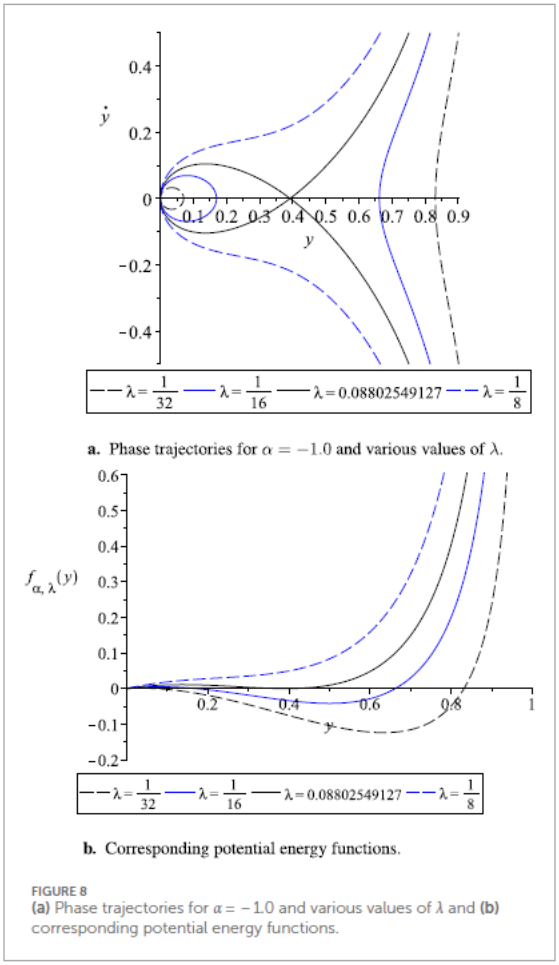

a. Phase trajectories for $\alpha = -1.0$ and various values of λ.

b. Corresponding potential energy functions.

FIGURE 8
(a) Phase trajectories for $\alpha = -1.0$ and various values of λ and (b) corresponding potential energy functions.

When the condition

$$h(y) = \frac{V_m^2}{(1-y)^2}$$

has a solution in the interval $(0,1)$, the system supports a periodic response. If this equation has no roots in $(-\infty, 1)$, then no periodic orbit exists, but if it has at least one real solution within $(-\infty, 1)$, the dynamics may still involve instability. Here, $V_m$and $V_M$denote the minimum and maximum amplitudes of the applied voltage $V(t)$, defined as

$$V_m = \min_{t\geq 0} | V(t) |, V_M = \max_{t\geq 0} | V(t) |.$$

Our nondimensional model in Eq. (39) corresponds to a particular case of Eq. (49), where $c = 0$and

$$h(y) = y + \alpha | y | y.$$

To verify the existence of periodic motion, let us introduce

$$\lambda_M = \max_{\tau\geq 0} | \lambda(\tau) |.$$

According to the theorem of Kadyrov et al., the nonautonomous nonlinear oscillator

$$\ddot{y} + y + \alpha | y | y - \frac{\lambda(\tau)}{(1-y)^2} = 0$$

admits a periodic solution whenever the equation

$$y + \alpha | y | y = \frac{\lambda_M}{(1-y)^2}$$

has a root in the interval $(0,1)$.

Define

$$f_\alpha(y) = (y + \alpha | y | y)(1-y)^2.$$

Since $y \in (0,1)$, the absolute value simplifies and we can write

$$f_\alpha(y) = (y + \alpha y^2)(1-y)^2, y \in [0,1). \qquad (50)$$

To find the turning points of $f_\alpha(y)$, we set its derivative equal to zero:

$$f'_\alpha(y) = 0.$$

This yields the critical values

$$y_{1,2} = \frac{2\alpha - 3 \pm \sqrt{4\alpha^2 + 4\alpha + 9}}{8\alpha}, y_3 = 1.$$

Using the second derivative test, it follows that $f_\alpha(y)$achieves a local maximum at the smaller of these critical points,

$$y_1 = \frac{2\alpha - 3 + \sqrt{4\alpha^2 + 4\alpha + 9}}{8\alpha}.$$

6 Simulation Results

6.1 Constant Voltage

In this part, we report numerical experiments of the normalized tip deflection $y(t)$as a function of nondimensional time. Different parameter sets with $\lambda > 0$and $\alpha < 0$were considered. All simulations were carried out using Maple™ software [38], and the outcomes are illustrated in Figures 10–13.

The results clearly demonstrate how the oscillation amplitude, frequency, and collapse time depend on the excitation parameter $\lambda$for fixed α. As λincreases, the tip displacement grows larger, and the oscillation period becomes longer. The maximum deflection amplitude is observed as λapproaches the separatrix threshold $\kappa(\alpha)$. In particular, the largest periodic trajectories correspond to excitations close to this boundary, specifically at $\lambda = \kappa(\alpha) - 10^{-3}$.

Additionally, decreasing αwhile keeping λconstant enhances both the amplitude and the oscillation period of $y(t)$. This indicates that system stiffness and nonlinearity strongly influence stability and response time.

6.2 Harmonic Voltage

We next turn to the **resonance response** of a graphene cantilever subject to a sinusoidal excitation. The forcing function is

$$V(t) = V_{\mathrm{DC}} + V_{\mathrm{AC}}\cos(\Omega t), \qquad (48)$$

where Ωis the forcing frequency. The system may undergo *primary resonance*—when Ωis close to the natural frequency—or *secondary resonances* at other excitation frequencies. Our focus here is on the primary case.

For the numerical study, we fixed $\alpha = -1.0$. The corresponding pull-in threshold for the excitation parameter is

$$\lambda^* = \kappa(\alpha) = 0.08802549127.$$

Recalling that

$$\lambda = \frac{\varepsilon_0 V_{\mathrm{DC}}^2 S}{2k_1(d + h/\varepsilon_r)^3},$$

we define

$$\beta = \frac{\varepsilon_0 S}{2k_1(d + h/\varepsilon_r)^3}.$$

For $\beta = 0.01$, the critical DC voltage becomes

$$V_{\mathrm{DC}} = \sqrt{\frac{\lambda^*}{\beta}} = 2.97. \qquad (51)$$

Thus, to avoid immediate static collapse, we chose $V_{\mathrm{DC}} = 2.5 < V_{\text{pull-in}}$and added a small harmonic perturbation $V_{\mathrm{AC}} = 0.1$.

From Eq. (47), the natural angular frequency for $V_{\mathrm{AC}} = 0$was computed as $\omega_n = 0.7391982714$. When Ωapproaches this value, the amplitude of the oscillations increases sharply. At exact resonance ($\Omega = \omega_n$), the tip deflection grows significantly, ultimately

leading to pull-in instability, where the free end touches the counter-electrode (Figures 14–15).

For comparison, simulations with $\Omega = 0$confirm stable periodic oscillations, since the parameter pair (α, λ)lies below the separatrix curve $\kappa(\alpha)$shown earlier in Figure 4.

Concluding Observations from Simulations

- Under **constant voltage**, the system is stable only if the parameters remain below the separatrix. Otherwise, pull-in collapse occurs.
- The deflection amplitude, frequency, and collapse time depend strongly on λ; the maximum amplitude arises just below the separatrix value for a given α.
- Under **harmonic excitation**, resonance can induce collapse even when the system parameters are below static pull-in thresholds.
- These findings emphasize the importance of precise modeling and parameter selection for MEMS graphene resonators.

Future work should focus on **experimental verification** and a comparative study of alternative lumped models. Because of graphene's unique nonlinear behavior, advanced mathematical methods—such as the homotopy perturbation approach [43–45]—offer promising tools for tackling the complexity of these systems, potentially outperforming conventional analytical techniques.

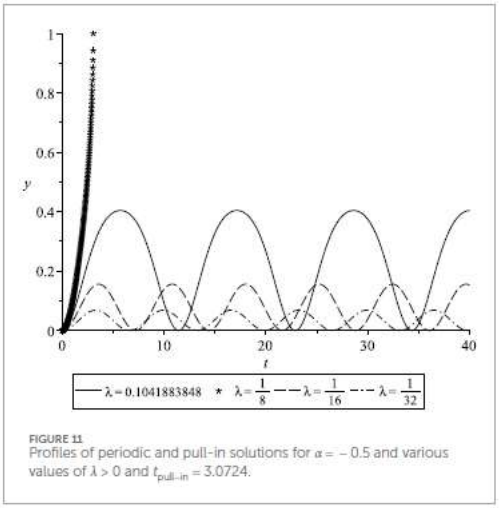

FIGURE 11
Profiles of periodic and pull-in solutions for $\alpha = -0.5$ and various values of $\lambda > 0$ and $t_{pull-in} = 3.0724$.

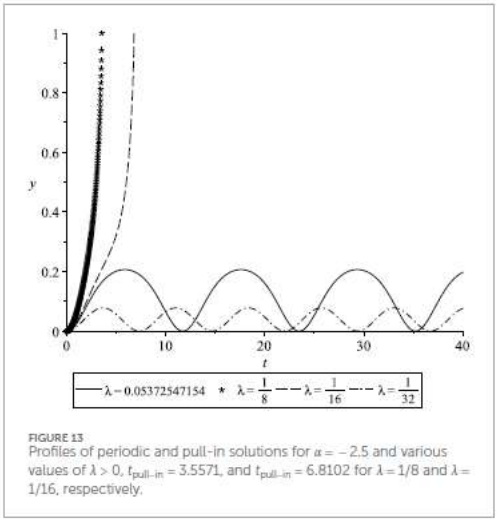

FIGURE 13
Profiles of periodic and pull-in solutions for $\alpha = -2.5$ and various values of $\lambda > 0$, $t_{pull-in} = 3.5571$, and $t_{pull-in} = 6.8102$ for $\lambda = 1/8$ and $\lambda = 1/16$, respectively.

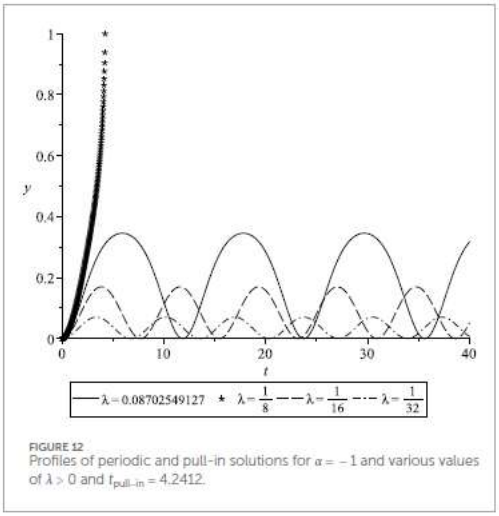

FIGURE 12
Profiles of periodic and pull-in solutions for $\alpha = -1$ and various values of $\lambda > 0$ and $t_{pull-in} = 4.2412$.

7. Conclusion and Outlook

This work presented an in-depth study of the static and dynamic responses of a graphene-based cantilever beam subjected to electrostatic loading at its free end. The nonlinear static formulation was first solved analytically, and its consistency with the classical linear beam solution was confirmed in the limiting case where the second-order elastic stiffness parameter Dtends to zero.

The subsequent analysis focused on the **dynamic pull-in instability** under both constant bias and harmonic excitation. The theoretical predictions were thoroughly compared with numerical simulations. For the constant voltage case, the model produced stable periodic

oscillations whenever the pair (α, λ)remained below the separatrix boundary, while exceeding this boundary inevitably led to collapse. The simulations further revealed how the excitation parameter λinfluences the amplitude, oscillation frequency, and time-to-pull-in for a fixed α. Notably, the largest stable oscillations occur just beneath the separatrix threshold.

When the system was driven by a harmonic load, the results demonstrated that operating close to the natural resonance frequency can destabilize the structure even when parameters are below the static pull-in limit. This shows that resonance effects must be carefully considered in the design of graphene MEMS devices, since dynamic collapse can occur under conditions that appear stable in static analysis.

The outcomes of this study provide valuable insights for the **design of MEMS resonators**. Future efforts should emphasize experimental validation, along with a systematic comparison of different lumped-mass models tailored to graphene structures. Because of the pronounced nonlinearities inherent in graphene resonators, accurate modeling tools are essential. Advanced analytical approaches, such as the **homotopy perturbation method** [43–45], hold significant promise for handling these complexities and may outperform classical approximation techniques in strongly nonlinear regimes.

References

1. Younis, M. I. *MEMS Linear and Nonlinear Statics and Dynamics.* Springer Science & Business Media, 2011.

2. Hanay, M. S., Kelber, S., Naik, A., Chi, D., Hentz, S., Bullard, E., et al. "Single-protein nanomechanical mass spectrometry in real time." *Nature Nanotechnology* 7, 602–608 (2012). doi:10.1038/nnano.2012.119

3. Jensen, K., Kim, K., & Zettl, A. "An atomic-resolution nanomechanical mass sensor." *Nature Nanotechnology* 3, 533–537 (2008). doi:10.1038/nnano.2008.200

4. Steele, G. A., Hüttel, A. K., Witkamp, B., Poot, M., Meerwaldt, H. B., Kouwenhoven, L. P., et al. "Strong coupling between single-electron tunneling and nanomechanical motion." *Science* 325, 1103–1107 (2009). doi:10.1126/science.1176076

5. Fuhrer, M. S., Lau, C. N., & MacDonald, A. H. "Graphene: materially better carbon." *MRS Bulletin* 35, 289–295 (2010). doi:10.1557/mrs2010.551

6. Pesin, D., & MacDonald, A. H. "Spintronics and pseudospintronics in graphene and topological insulators." *Nature Materials* 11(5), 409–416 (2012). doi:10.1038/nmat3305

7. Lee, J.-U., Yoon, D., & Cheong, H. "Estimation of Young's modulus of graphene by Raman spectroscopy." *Nano Letters* 12, 4444–4448 (2012). doi:10.1021/nl301073q

8. Li, Y. "Reversible wrinkles of monolayer graphene on a polymer substrate: toward stretchable and flexible electronics." *Soft Matter* 12, 3202–3213 (2016). doi:10.1039/c6sm00108d

9. Tomori, H., Kanda, A., Goto, H., Ootuka, Y., Tsukagoshi, K., Moriyama, S., et al. "Introducing nonuniform strain to graphene using dielectric nanopillars." *Applied Physics Express* 4, 075102 (2011). doi:10.1143/apex.4.075102

10. Khan, Z. H., Kermany, A. R., Öchsner, A., & Iacopi, F. "Mechanical and electromechanical properties of graphene and their potential application in MEMS."

Journal of Physics D: Applied Physics 50, 053003 (2017). doi:10.1088/1361-6463/50/5/053003

11. Rüegg, A., & Lin, C. "Bound states of conical singularities in graphene-based topological insulators." *Physical Review Letters* 110(4) (2013). doi:10.1103/physrevlett.110.046401

12. Wang, X., Tian, H., Xie, W., Shu, Y., Mi, W.-T., Mohammad, M. A., et al. "Observation of a giant two-dimensional band-piezoelectric effect on biaxial-strained graphene." *NPG Asia Materials* 7, e154 (2015). doi:10.1038/am.2014.124

13. Ghosh, S., Calizo, I., Teweldebrhan, D., Pokatilov, E. P., Nika, D. L., Balandin, A. A., et al. "Extremely high thermal conductivity of graphene: prospects for thermal management applications in nanoelectronic circuits." *Applied Physics Letters* 92 (2008). doi:10.1063/1.2907977

14. Balandin, A. A., Ghosh, S., Bao, W., Calizo, I., Teweldebrhan, D., Miao, F., et al. "Superior thermal conductivity of single-layer graphene." *Nano Letters* 8, 902–907 (2008). doi:10.1021/nl0731872

15. Iacopi, F., Brongersma, S., Vandevelde, B., O'Toole, M., Degryse, D., Travaly, Y., et al. "Challenges for structural stability of ultra-low-k-based interconnects." *Microelectronic Engineering* 75, 54–62 (2004). doi:10.1016/j.mee.2003.09.011

16. Dai, M. D., Kim, C.-W., & Eom, K. "Nonlinear vibration behavior of graphene resonators and their applications in sensitive mass detection." *Nanoscale Research Letters* 7, 499 (2012). doi:10.1186/1556-276x-7-499

17. Li, L., Yu, F., & Qin, Q. "Interaction and manipulation for non-autonomous bright soliton solution of the coupled derivative nonlinear Schrödinger equations with Riemann–Hilbert method." *Applied Mathematics Letters* 149 (2024). doi:10.1016/j.aml.2023.108924

18. Natsuki, T., Shi, J.-X., & Ni, Q.-Q. “Vibration analysis of nanomechanical mass sensor using double-layered graphene sheet resonators.” *Journal of Applied Physics* 114 (2013). doi:10.1063/1.4820522

19. Karličić, D., Kozić, P., Adhikari, S., Cajić, M., Murmu, T., & Lazarević, M. “Nonlocal mass-nanosensor model based on the damped vibration of single-layer graphene sheet influenced by in-plane magnetic field.” *International Journal of Mechanical Sciences* 96, 132–142 (2015). doi:10.1016/j.ijmecsci.2015.03.014

20. Wei, D., Liu, Y., & Elgindi, M. B. “Some analytic and finite element solutions of the graphene Euler beam.” *International Journal of Computer Mathematics* 91, 2276–2293 (2014). doi:10.1080/00207160.2013.871784

21. Anjum, N., & He, J.-H. “Nonlinear dynamic analysis of vibratory behavior of a graphene nano/microelectromechanical system.” *Mathematical Methods in the Applied Sciences* (2020). doi:10.1002/mma.6699

22. Kadyrov, S., Kashkynbayev, A., Skrzypacz, P., Kaloudis, K., & Bountis, A. “Periodic solutions and the avoidance of pull-in instability in nonautonomous microelectromechanical systems.” *Mathematical Methods in the Applied Sciences* 44, 14556–14568 (2021). doi:10.1002/mma.7725

23. Skrzypacz, P., Kadyrov, S., Nurakhmetov, D., & Wei, D. “Analysis of dynamic pull-in voltage of a graphene MEMS model.” *Nonlinear Analysis: Real World Applications* 45, 581–589 (2019). doi:10.1016/j.nonrwa.2018.07.025

24. Wei, D., Nurakhmetov, D., Aniyarov, A., Zhang, D., & Spitas, C. “Lumped-parameter model for dynamic monolayer graphene sheets.” *Journal of Sound and Vibration* 534, 117062 (2022). doi:10.1016/j.jsv.2022.117062

25. Omarov, D., Nurakhmetov, D., Wei, D., & Skrzypacz, P. “On the application of Sturm’s theorem to analysis of dynamic pull-in for a graphene-based MEMS model.” *Applied and Computational Mechanics* 12 (2018). doi:10.24132/acm.2018.413

26. Qing, Q., Li, L., & Fajun, Y. “Non-autonomous exact solutions and dynamic behaviors for the variable coefficient nonlinear Schrödinger equation with external potential.” *Physica Scripta* 100(1) (2024). doi:10.1088/1402-4896/ad9870

27. Varadan, V. K., Vinoy, K. J., & Jose, K. A. *RF MEMS and Their Applications.* John Wiley & Sons, 2003.

28. He, J.-H. “Periodic solution of a micro-electromechanical system.” *Facta Universitatis, Series Mechanical Engineering* (2024), 187–198. doi:10.22190/fume240603034h

29. He, J.-H., Yang, Q., He, C.-H., & Alsolami, A. A. “Pull-down instability of the quadratic nonlinear oscillators.” *Facta Universitatis, Series Mechanical Engineering* 21, 191–200 (2023). doi:10.22190/fume230114007h

30. Li, L., & Fajun, Y. “The fourth-order dispersion effect on the soliton waves and soliton stabilities for the cubic-quintic Gross–Pitaevskii equation.” *Chaos, Solitons & Fractals* 179 (2024). doi:10.1016/j.chaos.2023.114377

31. Skrzypacz, P., Wei, D., Nurakhmetov, D., Kostsov, E. G., Sokolov, A. A., Begzhigitov, M., et al. “Analysis of dynamic pull-in voltage and response time for a micro-electromechanical oscillator made of power-law materials.” *Nonlinear Dynamics* 105, 227–240 (2021). doi:10.1007/s11071-021-06653-3

32. Poggetto, V. F. D., Pal, R., Pugno, N., & Miniaci, M. “Topological bound modes in phononic lattices with nonlocal interactions.” *International Journal of Mechanical Sciences* 281 (2024). doi:10.1016/j.ijmecsci.2024.109503

33. Lee, C., Wei, X., Kysar, J. W., & Hone, J. “Measurement of the elastic properties and intrinsic strength of monolayer graphene.” *Science* 321, 385–388 (2008). doi:10.1126/science.1157996

34. Lu, Q., & Huang, R. “Nonlinear mechanics of single-atomic-layer graphene sheets.” *International Journal of Applied Mechanics* 1, 443–467 (2009). doi:10.1142/s1758825109000228

35. Khan, Z. H., Kermany, A. R., Öchsner, A., & Iacopi, F. “Mechanical and electromechanical properties of graphene and their potential application in MEMS.” *Journal of Physics D: Applied Physics* 50, 053003 (2017). doi:10.1088/1361-6463/50/5/053003
36. Meirovitch, L. *Fundamentals of Vibrations.* Waveland Press, Long Grove, Illinois, 2010.
37. Skrzypacz, P., Bountis, A., Nurakhmetov, D., & Kim, J. “Analysis of the lumped mass model for the cantilever beam subject to Grob’s swelling pressure.” *Communications in Nonlinear Science and Numerical Simulation* 85, 105230 (2020). doi:10.1016/j.cnsns.2020.105230
38. Maplesoft. *Maple User Manual.* Waterloo, Ontario: Maplesoft, a division of Waterloo Maple Inc., 1996.
39. Chen, Z., Gandhi, U., Lee, J., & Wagoner, R. “Variation and consistency of Young’s modulus in steel.” *Journal of Materials Processing Technology* 227, 227–243 (2016). doi:10.1016/j.jmatprotec.2015.08.024
40. Howatson, A. M. *Engineering Tables and Data.* Springer Science & Business Media, 2012.
41. Hopcroft, M. A., Nix, W. D., & Kenny, T. W. “What is the Young’s modulus of silicon?” *Journal of Microelectromechanical Systems* 19, 229–238 (2010). doi:10.1109/jmems.2009.2039697
42. Yajima, S., Okamura, K., & Hayashi, J. “Structural analysis in continuous silicon carbide fiber of high tensile strength.” *Chemistry Letters* 4, 1209–1212 (1975). doi:10.1246/cl.1975.1209
43. Moussa, B., Youssouf, M., Abdoul Wassiha, N., & Youssouf, P. “Homotopy perturbation method to solve Duffing–Van der Pol equation.” *Advances in Differential Equations and Control Processes* 31(3), 299–315 (2024). doi:10.17654/0974324324016
44. Alshomrani, N. A. M., Alharbi, W. G., Alanazi, I. M. A., Alyasi, L. S. M., Alrefaei, G. N. M., Al’amri, S. A., et al. “Homotopy perturbation method for solving a nonlinear system for an epidemic.” *Advances in Differential Equations and Control Processes* 31(3), 347–355 (2024). doi:10.17654/0974324324019
45. He, J.-H., He, C.-H., & Alsolami, A. A. “A good initial guess for approximating nonlinear oscillators by the homotopy perturbation method.” *Facta Universitatis, Series Mechanical Engineering* 21(1), 21–29 (2023).